

MATERIALS SCIENCE

Metallic line defect in wide-bandgap transparent perovskite BaSnO₃

Hwanhui Yun¹, Mehmet Topsakal², Abhinav Prakash^{1,3,4}, Bharat Jalan¹, Jong Seok Jeong^{1,5}, Turan Birol¹, K. Andre Mkhoyan^{1*}

A line defect with metallic characteristics has been found in optically transparent BaSnO₃ perovskite thin films. The distinct atomic structure of the defect core, composed of Sn and O atoms, was visualized by atomic-resolution scanning transmission electron microscopy (STEM). When doped with La, dopants that replace Ba atoms preferentially segregate to specific crystallographic sites adjacent to the line defect. The electronic structure of the line defect probed in STEM with electron energy-loss spectroscopy was supported by ab initio theory, which indicates the presence of Fermi level-crossing electronic bands that originate from defect core atoms. These metallic line defects also act as electron sinks attracting additional negative charges in these wide-bandgap BaSnO₃ films.

INTRODUCTION

In crystals, imperfections exist as various forms of defects covering a full dimensionality spectrum ranging from zero-dimensional (0D) point defects, such as vacancies and dopants, to more extended defects, such as 1D dislocations and disclinations, 2D grain boundaries and stacking faults, and, last, 3D voids and inclusions. Of particular interest for new technologies are extended 1D and 2D defects because they run across the macroscopic crystal in certain directions and are atomically small in others. Thus, they can provide nanoscale and, in some cases, atomic-scale tunability of material properties without altering the overall structure of the crystal (1). Perovskite crystals (ABX₃) have been shown to be suitable hosts for various conventional and nonconventional 1D and 2D defects with unexpected properties. A large diversity of elements can be incorporated at each of the three A, B, and X sites of perovskites, engendering with a wide range of phases and functionalities (2–4). Because the structure of perovskites, especially perovskite oxides, are highly flexible, it accommodates various types of distortions including octahedral BO₆ tilt (5, 6), uniaxial and biaxial strains (7), orbital ordering (8, 9), and cation ordering (10). The structural flexibility of perovskites allows formation of unique extended defects such as intrusion of related phases, e.g., Ruddlesden-Popper faults and phases (11, 12) or Aurivillius phase (13), nanorods, and line defects (14–16). Analytical atomic-resolution scanning transmission electron microscopes (STEMs) equipped with various spectrometers (17–19) are uniquely suitable for discovery of previously unidentified extended 1D and 2D defects and characterization of their atomic structure, composition, and electronic properties (15, 20–22). Here, using STEM imaging, energy-dispersive x-ray (EDX), and electron energy-loss spectroscopy (EELS), in combination with ab initio calculations, we report on the identification of a new kind of 1D line defect with metallic characteristics in otherwise transparent, wide-bandgap perovskite BaSnO₃ thin films. While only a few nonconventional (not dislocation or disclination type) line defects have been reported, e.g., a semi-

conducting line defect in insulating NdTiO₃ (15), the field of nonconventional line defects in perovskites is still largely unexplored but hugely promising.

Perovskite BaSnO₃ is one of the alkaline earth stannates (ASnO₃, A = Ca, Sr, and Ba) that has high optical transparency because of its wide bandgap of 3.0 ± 0.2 eV (23, 24). It also has high room temperature carrier mobility, reaching 320 cm² V⁻¹ s⁻¹ in a doped BaSnO₃ bulk crystal (25, 26) and 183 cm² V⁻¹ s⁻¹ in a doped BaSnO₃ thin film (27, 28) despite the presence of a considerable amount of crystalline defects. Typical extended defects, such as threading and misfit dislocations (28–30), grain boundaries (30), and Ruddlesden-Popper faults (29), are common in these perovskite BaSnO₃ films regardless of growth methods.

RESULTS AND DISCUSSION

The findings discussed here come from STEM-based experiments conducted on La-doped BaSnO₃ (La:BaSnO₃) films. Films grown with two different techniques, high-pressure oxygen sputtering and hybrid molecular beam epitaxy (MBE), were studied and almost all of them had the same metallic line defect in them. The low-magnification cross-sectional high-angle annular dark-field (HAADF)-STEM image of one of the La:BaSnO₃ films, grown on a LaAlO₃ substrate, shows the overall structure of the BaSnO₃ film (Fig. 1A). The contrast variations due to grain boundaries and dislocations can be seen throughout its thickness. At high resolution, due to considerable differences in atomic numbers between cations Ba ($Z_{\text{Ba}} = 56$), Sn ($Z_{\text{Sn}} = 50$), and anion O ($Z_{\text{O}} = 8$), HAADF-STEM images only show the atomic columns with cations in them, as seen in Fig. 1B. Because perovskite BaSnO₃ has a cubic crystal structure, projected HAADF-STEM images recorded along all three major axes ([001], [010], and [100]) show the same atomic column arrangement, if the film is fully relaxed.

In the high-resolution HAADF-STEM images of these BaSnO₃ films obtained in plan view, one of which is presented in Fig. 1C, the new line defects can be easily spotted because of their unique atomic configuration with a characteristic pair of atomic columns at the center. These line defects are observed only when viewed in the plan-view direction regardless of film growth technique, which indicates that they form preferentially along the growth direction suggesting possibilities for manipulations and control of the defects.

¹Department of Chemical Engineering and Materials Science, University of Minnesota, Minneapolis, MN 55455, USA. ²Nuclear Science and Technology Department, Center for Functional Nanomaterials, Brookhaven National Laboratory, Upton, NY 11973, USA. ³Pritzker School of Molecular Engineering, University of Chicago, Chicago, IL 60637, USA. ⁴Center for Nanoscale Materials, Argonne National Laboratory, Lemont, IL 60439, USA. ⁵Analytical Sciences Center, LG Chem Ltd., Daejeon, Republic of Korea. *Corresponding author. Email: mkhoyan@umn.edu

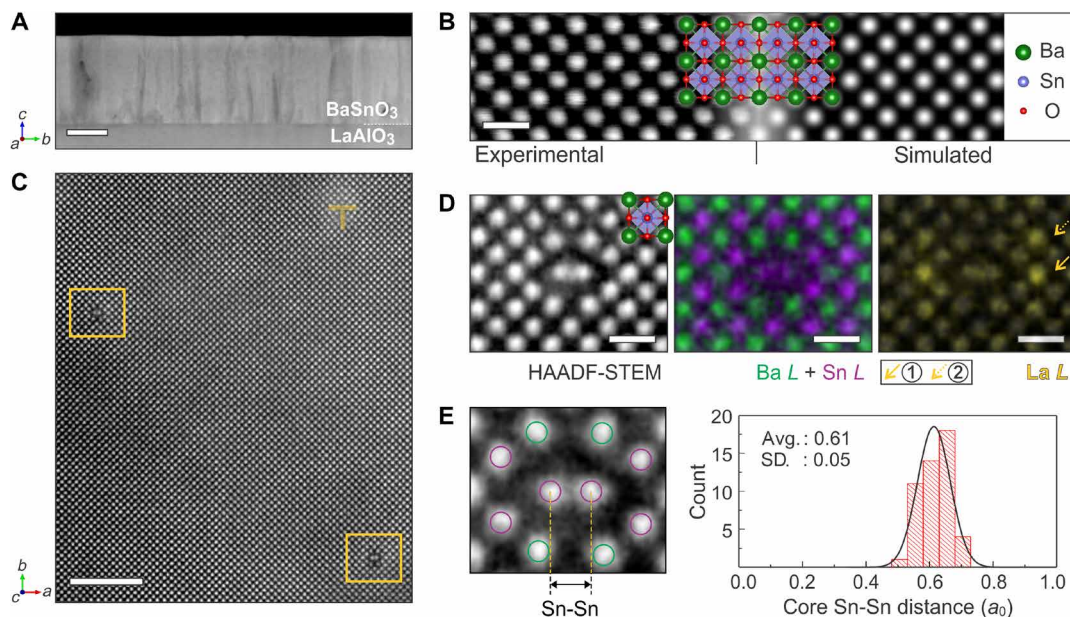


Fig. 1. HAADF-STEM images and EDX elemental maps of the line defect in perovskite BaSnO_3 . (A) Cross-sectional HAADF-STEM image of a BaSnO_3 film grown on a LaAlO_3 substrate. Scale bar, 100 nm. (B) Experimental and simulated atomic-resolution HAADF-STEM image of cubic BaSnO_3 viewed in the [001] direction. The overlaid polyhedral model shows the locations of the atoms in this projection. Scale bar, 0.5 nm. (C) Plan-view HAADF-STEM image of the BaSnO_3 film with two unique line defects (in the yellow boxes) and one edge dislocation (indicated by a dislocation symbol). Scale bar, 4 nm. (D) High-magnification HAADF-STEM image and EDX elemental maps superimposed on the HAADF-STEM image. Here, the sum of eight cross-correlated elemental maps is shown. Scale bars, 0.5 nm. (E) A close-up image of the defect core and histogram of the core Sn-Sn column distances relative to the lattice constant (a_0) of the host BaSnO_3 . The histogram is compiled from individual line defects across many samples. Precision of individual Sn-Sn distance measurement is $\pm 0.04a_0$.

Atomic-resolution STEM-EDX elemental maps (Fig. 1D) reveal the compositional details of the defect core and its surrounding (for details, see fig. S1). The two atomic columns at the center—the main visible feature of this defect—are Sn atomic columns (for additional examples of images and EDX maps of the line defects in sputtered and MBE grown films, see fig. S2). To form the defect core, it appears that two Ba columns should be absent and two Sn columns are “rotated” 90° along the [001] axis from their original (host) positions. Slight displacements of the four closest Ba columns toward the defect core to relax the strain in the structure are also observed (for details, see fig. S3). High concentrations of La dopants are detected at the specific Ba sites adjacent to the line defect. As can be seen from the La EDX map in Fig. 1D, La dopants are primarily substituting Ba atoms in the Ba columns just next to the core Sn-Sn pair, at the type ① sites, and less frequently, in Ba columns next to those, at the type ② sites (for more examples, see fig. S2). When defect core Sn-Sn pair distance was measured and compared to that in the host BaSnO_3 , which is the same as the lattice constant a_0 , it was found to be only about $0.61 \times a_0$ and had a range from 0.45 to $0.75 \times a_0$ (Fig. 1E).

An illustration of these line defects inside a BaSnO_3 film formed along the film growth direction (c axis) is shown in Fig. 2A. It should be noted that not all line defects necessarily propagate from a substrate to the film surface (see fig. S4). On the basis of the STEM observations, a one-unit cell-thick model for a basic atomic structure of the line defect was constructed. Then, the model was relaxed to its lowest-energy configuration by using *ab initio* calculations (for details, see Materials and Methods). For better insight into the structure of this line defect, several models with slight structural and compositional variations were considered, relaxed, and evalu-

ated: (i) without La dopants; (ii) with La dopants at sites ①, ②, and others; and (iii) with and without oxygen in between Sn-Sn pair in the core (for details, see figs. S5 and S6). The final relaxed structure of the simplest and the most representative model for the line defect is shown in Fig. 2B viewed in three main projections. In this simplified model, La dopants are substituting all Ba atoms at the sites type ① and the sites type ② are free of La. After the structural relaxation, the two core Sn atomic columns are shifted a half-unit cell along the line defect direction ([001]), which is visible when viewed from [100] and [010] directions. The distance between core Sn-Sn atomic columns is also reduced and four adjacent Ba columns are moved inward, both of which are consistent with the experimental observations (see also fig. S3). The agreement between this model and STEM measurements appears to be fairly good, including a close match of the core Sn-Sn distance in the relaxed structure ($0.72 \times a_0$) to experimentally observed values.

Using this simple model for atomic structure, the electronic band structure of the line defect was calculated using density functional theory (DFT), and defect-induced electronic bands crossing the Fermi level, E_F , were observed, as illustrated in Fig. 2C. The resulting band structure and total and atom-projected density of states (DOS) are shown in Fig. 2D. A few defect-induced electronic bands (highlighted in red) are partially filled as they cross the Fermi level, $E_F = 0$, which implies the presence of metallic electronic states in the line defect. In addition to these bands, there are also other unfilled, defect-induced, distinct bands spanning from 0.2 to 1.3 eV that are not present in bulk BaSnO_3 (31). While atom-projected DOS reveals that the metallic states are originated from O and Sn atoms in the structure (Fig. 2D), site-projected DOS of individual Sn and O atoms in the structure helps to identify the sites responsible for metallic

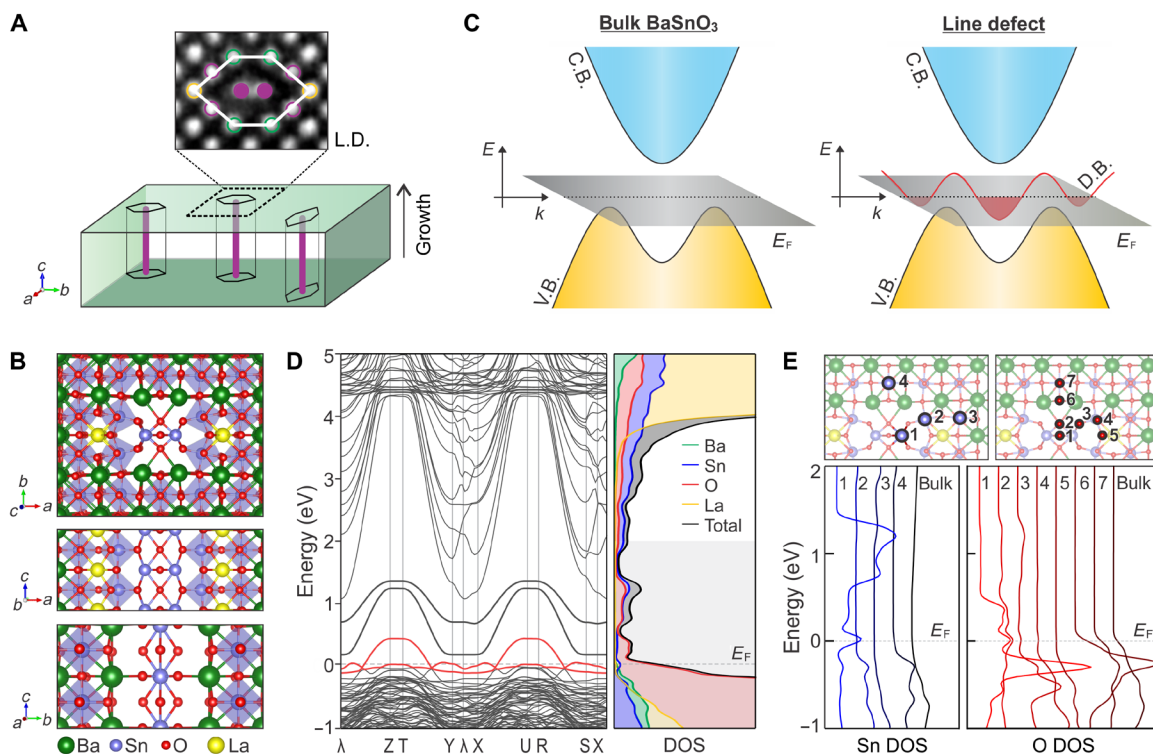


Fig. 2. Computed atomic and electronic structures of the line defect. (A) An illustration of line defects (L.D.) in BaSnO₃ thin film forming along the film growth direction. (B) Calculated atomic structure of the line defect viewed along the three major axes. Here, La atoms acting as substitutional dopants are shown in yellow occupying Ba sites neighboring the defect core. The Sn atoms in the defect core are shifted a half-unit cell along the defect line direction. The calculations also predict minor changes in the atomic structure of the BaSnO₃ structure outside the defect core (e.g., an octahedral tilt in the four surrounding four SnO₆ octahedra when viewed in the *c* direction). (C) Schematic band diagrams of BaSnO₃ illustrating the band from the line defect crossing E_F . (D) Electronic band structures and DOS of the line defect calculated using atomic structure in (B). Metallic bands, the bands that are crossing Fermi energy ($E_F = 0$), are highlighted in red. Atom-projected DOS indicate that the metallic bands are predominantly from O and Sn atoms. (E) Site-projected DOS for Sn and O atoms in the line defect structure. The DOS of selected atoms, locations of which are indicated in the schematics on the top, show that the O and Sn atoms of the defect core are the ones with metallic characteristics.

bands. As shown in Fig. 2E, the metallic bands that are crossing the Fermi level originated primarily from Sn and O atoms in the defect core: Sn-1, O-1, O-2, and O-3. These results appear to be the direct consequence of considerable differences between the coordination and bond angles for the core O and Sn atoms than those in the host perovskite BaSnO₃ (e.g., Sn-O-Sn angle is 74° and 58° in the core and 180° in the host). Electronic structure calculations conducted for the line defect without La dopants (see fig. S7) and for the line defect with an O vacancy (see fig. S8) also showed a metallic defect core with similar results for band structure and DOS, suggesting that being metallic is most likely an intrinsic property of these line defects in BaSnO₃.

Because these metallic line defects are imbedded inside an n-type doped insulating BaSnO₃ host (32) (each La dopant provides one extra electron when it substitutes Ba atom), some changes in atomic and electronic structures are expected when an extra negative charge is introduced into the system. A set of calculations for structure optimization with different amounts of added negative charge (number of electrons) was performed. It revealed that an increase of additional negative charge decreases the Sn-Sn distance at the core, bringing the structure even closer to the ones observed in experiments (Fig. 3A). A reduction of core Sn-Sn distance was observed for both line defects with and without La dopants. Because the line defects in the different films have different amounts of surrounding

dopants and additional negative charges in them, that would explain the experimentally observed variation of Sn-Sn distances in the core discussed earlier (Fig. 1E).

The electron density distributions of these negatively charged line defects were calculated and compared with those of the original line defect to visualize the sites where the additional charge accumulates. The electron density maps for La-doped line defects with and without two added electrons were calculated using relaxed atomic structures with additional electrons; then, an electron density difference map (EDDM) was constructed. The EDDMs for the two crystalline planes (BaO and SnO₂ planes) perpendicular to the defect line are shown in Fig. 3B. They indicate that the additional electrons are filling the available states in the Sn and O atoms at the defect core, which is consistent with their metallic characteristics—having localized electronic states that are crossing the Fermi level. These line defects appear to act as electron sinks attracting additional negative charges in the film. The EDDMs also provide a real-space visualization of the changes in the electronic orbitals of the atoms that are contributing to the band structure. The characteristic lobes of filled O 2*p* orbitals are clearly visible in the EDDM of the SnO₂ plane (Fig. 3B), where the effects of the orbital hybridization due to bonding are minimal. The EDDMs calculated for the line defect without La dopants, which is also metallic, show similar defect core-concentrated distribution of the additional electrons (see fig. S9).

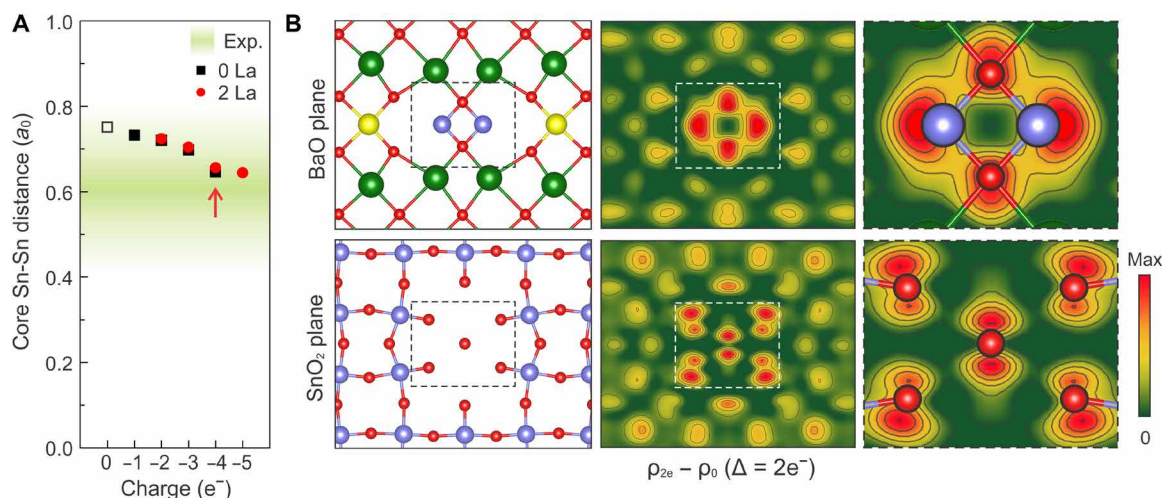


Fig. 3. The effect of an additional negative charge on the line defect. (A) Calculated core Sn-Sn distance of the line defect as a function of negative charge added to the structure. Both cases, undoped (0 La) and La substitutional doped (2 La), are considered. In the doped case, the structure already has $2e^-$ charge because each La ($Z_{\text{La}}=57$) introduces one extra electron when it substitutes Ba ($Z_{\text{Ba}}=56$). (B) The atomic arrangements (on the left) and corresponding EDDMs between the additionally charged (with $2e^-$) and original line defects for both atomic planes perpendicular to the defect line direction (on the right). Magnified EDDMs of the defect core with overlaid atom positions show that most of the additional charge is concentrated at the core O and Sn atoms. The structure used for calculating these EDDMs is indicated by the arrow in (A).

EELS core-loss edges are directly related to the local DOS above the Fermi energy of the material and can be acquired in STEM at atomic resolution in parallel with imaging (33, 34); therefore, it is an excellent method for experimental investigation of the local electronic structure of extended 1D and 2D defects. To determine the applicability of the core-level EELS for this line defect, the spectral shapes of O *K* edge, the most sensitive EELS edge in BaSnO₃, were simulated for different oxygen atoms in the line defect structure. The calculations were based on electronic band structure and DOS (Figs. 2, D and E) with incorporation of the core-hole effect. The results, presented in Fig. 4A, indicate that the *K* edge fine structures of the oxygen atoms at the defect sites are drastically different. In particular, three oxygen atoms at the defect core (sites O-1, O-2, and O-3 in Fig. 4A) exhibit a peak at the edge onset, which is due to metallic states in the band structure crossing the Fermi energy, as discussed earlier. This and other visible changes in *K* edge fine structures of oxygen atoms in the defect core suggest that experimental EELS should be applicable here. However, because of STEM probe channeling and broadening (35) during its propagation through the sample (Fig. 4B), some intermixing of these simulated O *K* edges is expected in measured EELS data.

EELS O *K* edges were acquired across the line defects along two perpendicular directions: vertical (i) and parallel (ii) to the characteristic core Sn-Sn pair (Fig. 4C). The changes in the O *K* edge fine structures are localized within a few unit cells from the defect. For O *K* edges acquired along direction i, the changes in the fine structure at the defect core (region i0) relative to that of host BaSnO₃ (bulk, b) are readily observed. They are more pronounced in the difference spectrum (Fig. 4C). For comparison, the difference spectrum between the O *K* edges from the region i3, a three unit cell away from the core, and bulk shows only noise signals. At the defect core, the intensity near the onset (shaded 530 to 533.5 eV range) is enhanced, which is consistent with the presence of metallic states at the defect and with simulated edge predictions. In addition, peaks at

538.6, 539.9, 542.5, and 545.0 eV present in the host crystal are dampened at the defect core, which is also consistent with simulated O *K* edges (Fig. 4A). EELS data acquired along direction ii show similar results due to beam broadening and the intermixing of O *K* edges. The only difference here is in the region ii1, where the presence of La dopants causes formation of additional electronic states around 5 eV above the Fermi level at neighboring oxygen atoms (sites O-4 and O-5 in Fig. 4A).

When the difference spectrum from measured and simulated O *K* edges is compared (Fig. 4C), a good agreement is observed. The simulated O *K* edges used here for direct comparison with measured edges include effects of intermixing due to beam channeling and broadening (for details, see fig. S10). It should be noted that an even better match with experimental data might be achieved if simulated O *K* edges not only were based on the simple model of the line defect with two La dopants (Fig. 2B) but also include what was observed in actual films; that is, some portion of the defect does not have dopants at all and some La dopants are on other sites (Fig. 1D), and extra electrons can be accumulated at the defect core. Again, the simple model of the line defect appears to be sufficient to describe the essential properties of this metallic line defect.

The discovery of oxide metallic line defects in otherwise wide-bandgap transparent perovskite BaSnO₃ films demonstrates that extended 1D defects can accommodate remarkable properties and provide unique means for engineering material properties at the subnanometer length scale. Controlling the distribution and orientations of such line defects offers exciting opportunities for developing superior crystalline materials with extraordinary properties, including unidirectional metallic conductivity with simultaneous insulating character in orthogonal directions. Exploration of extended 1D defects beyond dislocations in perovskites is a mostly uncharted field where unexpected defect properties and new physical phenomena at atomic dimensions are waiting to be discovered.

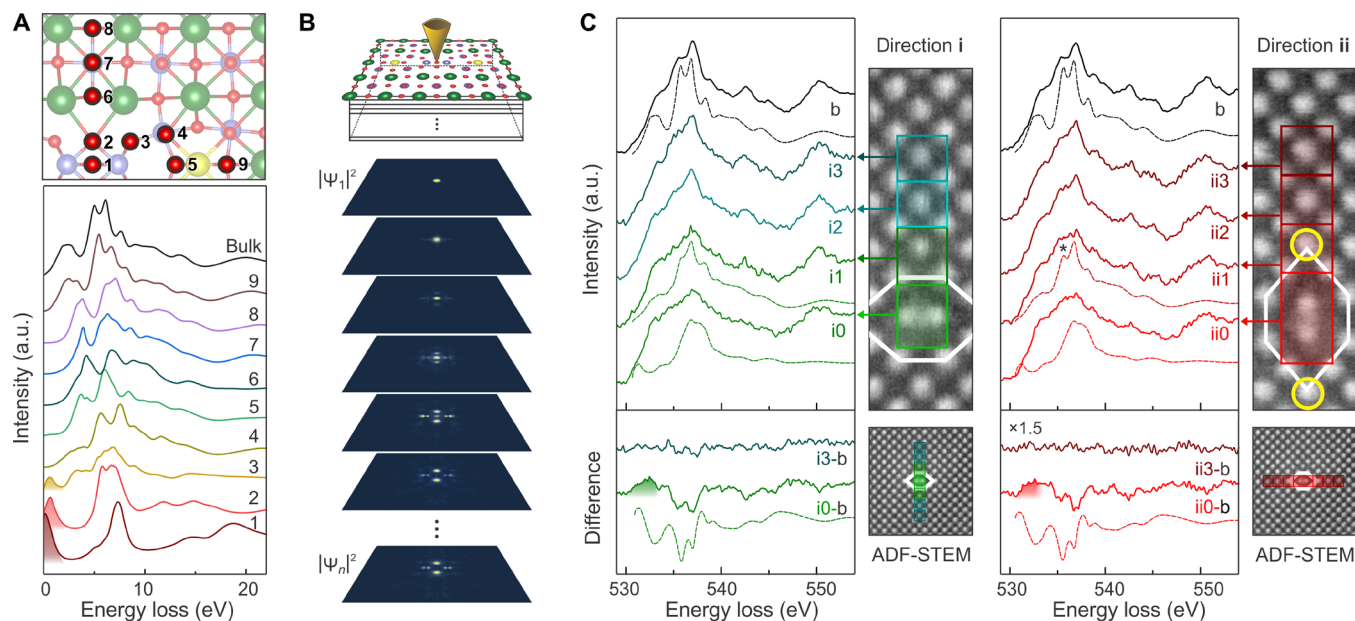


Fig. 4. EELS core-loss O K edges of the line defect. (A) Calculated O K edges for different O atoms in the line defect structure. The locations of these O atoms in the structure are indicated on the top panel. Peaks originated from metallic electronic states just above Fermi energy are highlighted with shading. a.u., arbitrary units. (B) A schematic showing that when the STEM probe is located on an individual atomic column, by the time the beam propagates and exits the sample, it broadens and, therefore, measured EELS data should contain excitations from neighboring atomic columns. (C) Measured and simulated O K edges across the line defect in two perpendicular directions (i and ii). EELS acquisition areas are indicated on the right. The solid lines and dashed lines represent experimental data and simulations, respectively. Label “b” indicates bulk. Enhanced peak due to bonding with La is marked with an asterisk. Simulated edges contain intermixing from neighboring oxygen atoms. Difference spectra between local and bulk O K edge spectra are shown in the bottom. Features corresponding to metallic electronic states just above Fermi energy are highlighted with shading.

MATERIALS AND METHODS

STEM characterization

La:BaSnO₃ films were grown on a LaAlO₃(001)_{pc} substrate by using high-pressure oxygen sputter deposition (36) and on LaAlO₃(001)_{pc} and SrTiO₃(001) substrates by hybrid MBE (37). La:BaSnO₃ films were grown on pseudo-cubic LaAlO₃(001)_{pc} and SrTiO₃(001) substrates. Plan-view STEM samples were prepared by mechanical polishing (using Multiprep, Allied High Tech Inc.) followed by colloidal polishing with alumina abrasives to thin the foil and to reduce damaged layers on the surfaces. The thickness of the area for STEM experiments was 40 to 90 nm and ~40 nm for plan-view and cross-sectional view samples, respectively. Cross-sectional TEM samples were prepared by the focus ion-beam lift-out method using a 30-kV Ga ion beam followed by ion shower at a 2-kV Ga ion beam.

STEM experiments were performed using aberration-corrected FEI Titan G2 60-300 (S)TEM equipped with a CEOS DCOR probe corrector, a Schottky extreme field emission gun, a monochromator, a super-X EDX detector, and a Gatan Enfinitum ER spectrometer. The microscope was operated at 200 keV and a screen current of 25 to 30 pA. STEM images and EDX elemental map were acquired using the probe semiconvergent angle of 17.3 mrad, and ADF detector inner angles of 55 and 11 mrad for HAADF-STEM and annular bright-field (ABF)-STEM images, respectively. STEM-EELS analysis was conducted using a monochromated probe allowing the energy resolution of 0.13 eV at the energy dispersion of 0.01 eV. The core-loss O K edges were acquired using the energy dispersion of 0.1 eV. Probe semiconvergent angle was 19 mrad, and EELS collection angle was 29 mrad. Dual EELS mode was used to acquire the low-loss

energy region with zero-loss peak (ZLP) and the high-loss energy region simultaneously, which allows energy drift correction using the ZLP alignment. The thicknesses of samples were determined from measured low-loss EELS spectra using the log-ratio method with the mean free paths of plasmon excitation $\lambda_p = 81$ nm for BaSnO₃ (38).

DFT simulations

The defect structure was obtained by fully relaxing the atomic coordinates and the lattice vectors, using the variable cell (vc-relax) option implemented in the Quantum-Espresso program package (39). Initial line defect structure was constructed using the supercell of $5 \times 4 \times 1$ unit cell (u.c.), where two Ba atoms were removed and two Sn atoms were displaced by 90° rotation along the [001] axis at the center of the supercell. Ultrasoft pseudopotentials (40) and a generalized gradient approximation (GGA) using Perdew-Burke-Ernzenhof (PBE) parameterization for an exchange-correlation functional were used (41). Kinetic energy cutoff for wave functions and for charge density was 50 and 200 Ry, respectively. Relaxation was achieved by converging the forces on all atoms to less than 1×10^{-4} atomic units. A k -point grid of $2 \times 2 \times 6$ was used. Atomic structure visualization in figures was performed using VESTA software (42).

Electronic structures and EELS simulations for the relaxed structures were carried out using the WIEN2K code (43–45). GGA-PBE parameterization was adopted for the electronic exchange-correlation functional (41). The Brillouin zone was sampled using a $4 \times 4 \times 16$ shifted k -point grid. R_{MT} (muffin tin radius) that was automatically set by the code was used, which was 2.45 Å (the structure without La dopant) and 2.5 Å (the structure with La dopant) for Ba, 2.04 Å for Sn, 1.75 Å for O, and 2.49 Å for La. The basis set cutoff wave vector,

k_{\max} was determined by the criterion $R_{\min}k_{\max} = 7$. Ground state electronic structures for charged line defects were calculated by adding electrons and adding corresponding background charge. Spin-orbit interactions were also included. EELS O K edge simulations were performed by using the TELNES3 module in WIEN2K with parameters identical to the experimental setup. To include the core-hole effects (46, 47), the bigger supercell structure for the line defect was generated by doubling the relaxed line structures in the [001] direction, which is compatible to the size of $5 \times 4 \times 2$ u.c., and then, core-hole was incorporated in an absorbing oxygen atom. O K edge for the host BaSnO₃ (bulk) was computed using the BaSnO₃ supercell with a size of $5 \times 4 \times 2$ u.c. The natural energy broadening of the core edges, caused by the lifetime of the electrons in the initial and final states of excitation, was incorporated as well (38, 48, 49).

STEM simulations

STEM image and STEM probe propagation simulations were performed using the TEMSIM code based on the Multislice method (50–52). To simulate the HAADF- and ABF-STEM images of the line defect, the relaxed line defect structure with two La dopants was used, which has a supercell size of $a = 21.01 \text{ \AA}$, $b = 16.53 \text{ \AA}$, and $c = 4.11 \text{ \AA}$. The STEM probe parameters were as follows: a beam energy of 200 keV, a convergence angle of 17.3 mrad (STEM image) and 19 mrad (electron beam propagation), $C_s = 0$, and a slice thickness of 2.055 Å. Thermal diffuse scattering was included using frozen-phonon approximation for $T = 300 \text{ K}$ (51). Root mean square thermal displacements were set as 0.095 Å for Ba, 0.1 Å for Sn, 0.089 Å for O, and 0.041 Å for La (53). Inner/outer detector angles for the HAADF- and ABF-STEM images were 50/200 and 10/40 mrad. The computed STEM images were convoluted with a Gaussian function with the full width at half maximum of 0.8 Å to incorporate the source size (54).

SUPPLEMENTARY MATERIALS

Supplementary material for this article is available at <http://advances.sciencemag.org/cgi/content/full/7/3/eabd4449/DC1>

REFERENCES AND NOTES

- B. G. Yacobi, D. B. Holt, *Extended Defects in Semiconductors* (Cambridge Univ. Press, 2007).
- J. B. Goodenough, Electronic and ionic transport properties and other physical aspects of perovskites. *Rep. Prog. Phys.* **67**, 1915–1993 (2004).
- H. N. Lee, H. M. Christen, M. F. Chisholm, C. M. Rouleau, D. H. Lowndes, Strong polarization enhancement in asymmetric three-component ferroelectric superlattices. *Nature* **433**, 395–399 (2005).
- D. Lee, H. Lu, Y. Gu, S.-Y. Choi, S.-D. Li, S. Ryu, T. R. Paudel, K. Song, E. Mikheev, S. Lee, S. Stemmer, D. A. Tenne, S. H. Oh, E. Y. Tsybmal, X. Wu, L.-Q. Chen, A. Gruverman, C. B. Eom, Emergence of room-temperature ferroelectricity at reduced dimensions. *Science* **349**, 1314–1317 (2015).
- T. H. Kim, D. Puggioni, Y. Yuan, L. Xie, H. Zhou, N. Campbell, P. J. Ryan, Y. Choi, J. W. Kim, J. R. Patzner, S. Ryu, J. P. Podkaminer, J. Irwin, Y. Ma, C. J. Fennie, M. S. Rzchowski, X. Q. Pan, V. Gopalan, J. M. Rondinelli, C. B. Eom, Polar metals by geometric design. *Nature* **533**, 68–72 (2016).
- T. Nan, T. J. Anderson, J. Gibbons, K. Hwang, N. Campbell, H. Zhou, Y. Q. Dong, G. Y. Kim, D. F. Shao, T. R. Paudel, N. Reynolds, X. J. Wang, N. X. Sun, E. Y. Tsybmal, S. Y. Choi, M. S. Rzchowski, Y. B. Kim, D. C. Ralph, C. B. Eom, Anisotropic spin-orbit torque generation in epitaxial SrTiO₃ by symmetry design. *Proc. Natl. Acad. Sci. U.S.A.* **116**, 16186–16191 (2019).
- J. H. Haeni, P. Irvin, W. Chang, R. Uecker, P. Reiche, Y. L. Li, S. Choudhury, W. Tian, M. E. Hawley, B. Craigo, A. K. Tagantsev, X. Q. Pan, S. K. Streiffer, L. Q. Chen, S. W. Kirchoefer, J. Levy, D. G. Schlom, Room-temperature ferroelectricity in strained SrTiO₃. *Nature* **430**, 758–761 (2004).
- Y. Yuan, Y. Lu, G. Stone, K. Wang, C. M. Brooks, D. G. Schlom, S. B. Sinnott, H. Zhou, V. Gopalan, Three-dimensional atomic scale electron density reconstruction of octahedral tilt epitaxy in functional perovskites. *Nat. Commun.* **9**, 5220 (2018).
- J. B. Goodenough, J.-S. Zhou, Orbital ordering in orthorhombic perovskites. *J. Mater. Chem.* **17**, 2394–2405 (2007).
- G. King, P. M. Woodward, Cation ordering in perovskites. *J. Mater. Chem.* **20**, 5785–5796 (2010).
- C.-H. Lee, N. D. Orloff, T. Birol, Y. Zhu, V. Goian, E. Rocas, R. Haislmaier, E. Vlahos, J. A. Mundy, L. F. Kourkoutis, Y. Nie, M. D. Biegalski, J. Zhang, M. Bernhagen, N. A. Benedek, Y. Kim, J. D. Brock, R. Uecker, X. X. Xi, V. Gopalan, D. Nuzhnyy, S. Kamba, D. A. Muller, I. Takeuchi, J. C. Booth, C. J. Fennie, D. G. Schlom, Exploiting dimensionality and defect mitigation to create tunable microwave dielectrics. *Nature* **502**, 532–536 (2013).
- G. Stone, C. Ophus, T. Birol, J. Ciston, C.-H. Lee, K. Wang, C. J. Fennie, D. G. Schlom, N. Alem, V. Gopalan, Atomic scale imaging of competing polar states in a Ruddlesden-Popper layered oxide. *Nat. Commun.* **7**, 12572 (2016).
- B. Frit, J. P. Mercurio, The crystal chemistry and dielectric properties of the Aurivillius family of complex bismuth oxides with perovskite-like layered structures. *J. Alloys Compd.* **188**, 27–35 (1992).
- I. MacLaren, L. Q. Wang, B. Schaffer, Q. M. Ramasse, A. J. Craven, S. M. Selbach, N. A. Spaldin, S. Miao, K. Kalantari, I. M. Reaney, Novel nanorod precipitate formation in neodymium and titanium codoped bismuth ferrite. *Adv. Funct. Mater.* **23**, 683–689 (2013).
- J. S. Jeong, M. Topsakal, P. Xu, B. Jalan, R. M. Wentzcovitch, K. A. Mkhoyan, A new line defect in NdTiO₃ perovskite. *Nano Lett.* **16**, 6816–6822 (2016).
- C. Li, D. Song, M. Li, C. Tang, D. Xue, D. Wan, S. J. Pennycook, Atomic scale characterization of point and extended defects in niobate thin films. *Ultramicroscopy* **203**, 82–87 (2019).
- M. Bosman, V. J. Keast, J. L. Garcia-Muñoz, A. J. D'Alfonso, S. D. Findlay, L. J. Allen, Two-dimensional mapping of chemical information at atomic resolution. *Phys. Rev. Lett.* **99**, 086102 (2007).
- D. A. Muller, L. F. Kourkoutis, M. Murfitt, J. H. Song, H. Y. Hwang, J. Silcox, N. Dellby, O. L. Krivanek, Atomic-scale chemical imaging of composition and bonding by aberration-corrected microscopy. *Science* **319**, 1073–1076 (2008).
- A. J. D'Alfonso, B. Freitag, D. Klenov, L. J. Allen, Atomic-resolution chemical mapping using energy-dispersive x-ray spectroscopy. *Phys. Rev. B* **81**, 100101 (2010).
- R. F. Klie, J. P. Buban, M. Varela, A. Franceschetti, C. Jooss, Y. Zhu, N. D. Browning, S. T. Pantelides, S. J. Pennycook, Enhanced current transport at grain boundaries in high-Tc superconductors. *Nature* **435**, 475–478 (2005).
- Z. Zhang, W. Sigle, W. Kurtz, HRTEM and EELS study of screw dislocation cores in SrTiO₃. *Phys. Rev. B* **69**, 144103 (2004).
- P. Gao, R. Ishikawa, B. Feng, A. Kumamoto, N. Shibata, Y. Ikuhara, Atomic-scale structure relaxation, chemistry and charge distribution of dislocation cores in SrTiO₃. *Ultramicroscopy* **184**, 217–224 (2018).
- H. J. Kim, U. Kim, T. H. Kim, J. Kim, H. M. Kim, B.-G. Jeon, W.-J. Lee, H. S. Mun, K. T. Hong, J. Yu, K. Char, K. H. Kim, Physical properties of transparent perovskite oxides (Ba,La)SnO₃ with high electrical mobility at room temperature. *Phys. Rev. B* **86**, 165205 (2012).
- S. A. Chambers, T. C. Kaspar, A. Prakash, G. Haugstad, B. Jalan, Band alignment at epitaxial BaSnO₃/SrTiO₃(001) and BaSnO₃/LaAlO₃(001) heterojunctions. *Appl. Phys. Lett.* **108**, 152104 (2016).
- X. Luo, Y. S. Oh, A. Sirenko, P. Gao, T. A. Tyson, K. Char, S.-W. Cheong, High carrier mobility in transparent Ba_{1-x}La_xSnO₃ crystals with a wide band gap. *Appl. Phys. Lett.* **100**, 172112 (2012).
- H. J. Kim, U. Kim, H. M. Kim, T. H. Kim, H. S. Mun, B. G. Jeon, K. T. Hong, W. J. Lee, C. Ju, K. H. Kim, K. Char, High mobility in a stable transparent perovskite oxide. *Appl. Phys. Express* **5**, 061102 (2012).
- S. Raghavan, T. Schumann, H. Kim, J. Y. Zhang, T. A. Cain, S. Stemmer, High-mobility BaSnO₃ grown by oxide molecular beam epitaxy. *APL Mater.* **4**, 016106 (2016).
- H. Paik, Z. Chen, E. Lochocki, A. H. Seidner, A. Verma, N. Tanen, J. Park, M. Uchida, S. Shang, B.-C. Zhou, M. Brützmam, R. Uecker, Z.-K. Liu, D. Jena, K. M. Shen, D. A. Muller, D. G. Schlom, Adsorption-controlled growth of La-doped BaSnO₃ by molecular-beam epitaxy. *APL Mater.* **5**, 116107 (2017).
- W. Y. Wang, Y. L. Tang, Y. L. Zhu, J. Suriyaparakash, Y. B. Xu, Y. Liu, B. Gao, S. W. Cheong, X. L. Ma, Atomic mapping of Ruddlesden-Popper faults in transparent conducting BaSnO₃-based thin films. *Sci. Rep.* **5**, 16097 (2015).
- H. Yun, K. Ganguly, W. Postiglione, B. Jalan, C. Leighton, K. A. Mkhoyan, J. S. Jeong, Microstructure characterization of BaSnO₃ thin films on LaAlO₃ and PrScO₃ substrates from transmission electron microscopy. *Sci. Rep.* **8**, 10245 (2018).
- E. Moreira, J. M. Henriques, D. L. Azevedo, E. W. S. Caetano, V. N. Freire, U. L. Fulco, E. L. Albuquerque, Structural and optoelectronic properties, and infrared spectrum of cubic BaSnO₃ from first principles calculations. *J. Appl. Phys.* **112**, 043703 (2012).
- A. Prakash, P. Xu, A. Faghaninia, S. Shukla, J. W. Ager III, C. S. Lo, B. Jalan, Wide bandgap BaSnO₃ films with room temperature conductivity exceeding 10⁴ S cm⁻¹. *Nat. Commun.* **8**, 15167 (2017).
- D. A. Muller, D. J. Singh, J. Silcox, Connections between the electron-energy-loss spectra, the local electronic structure, and the physical properties of a material: A study of nickel aluminum alloys. *Phys. Rev. B* **57**, 8181–8202 (1998).

34. L. J. Allen, S. D. Findlay, M. P. Oxley, Simulation and interpretation of images, in *Scanning Transmission Electron Microscopy: Imaging and Analysis*, S. J. Pennycook, P. D. Nellist, Eds. (Springer, 2011), pp. 247–289.
35. R. J. Wu, A. Mittal, M. L. Odlyzko, K. A. Mkhoyan, Simplifying electron beam channeling in scanning transmission electron microscopy (STEM). *Microsc. Microanal.* **23**, 794–808 (2017).
36. K. Ganguly, P. Ambwani, P. Xu, J. S. Jeong, K. A. Mkhoyan, C. Leighton, B. Jalan, Structure and transport in high pressure oxygen sputter-deposited BaSnO_{3-δ}. *APL Mater.* **3**, 062509 (2015).
37. A. Prakash, J. Dewey, H. Yun, J. S. Jeong, K. A. Mkhoyan, B. Jalan, Hybrid molecular beam epitaxy for the growth of stoichiometric BaSnO₃. *J. Vac. Sci. Technol. A* **33**, 060608 (2015).
38. R. F. Egerton, *Electron Energy Loss Spectroscopy in the Electron Microscope* (Springer, ed. 3, 2011).
39. P. Giannozzi, S. Baroni, N. Bonini, M. Calandra, R. Car, C. Cavazzoni, D. Ceresoli, G. L. Chiarotti, M. Cococcioni, I. Dabo, A. D. Corso, S. de Gironcoli, S. Fabris, G. Fratesi, R. Gebauer, U. Gerstmann, C. Gougoussis, A. Kokalj, M. Lazzeri, L. Martin-Samos, N. Marzari, F. Mauri, R. Mazzarello, S. Paolini, A. Pasquarello, L. Paulatto, C. Sbraccia, S. Scandolo, G. Sclauzero, A. P. Seitsonen, A. Smogunov, P. Umari, R. M. Wentzcovitch, QUANTUM ESPRESSO: A modular and open-source software project for quantum simulations of materials. *J. Phys. Condens. Matter* **21**, 395502 (2009).
40. K. F. Garrity, J. W. Bennett, K. M. Rabe, Pseudopotentials for high-throughput DFT calculations. *Comput. Mater. Sci.* **81**, 446–452 (2014).
41. J. P. Perdew, K. Burke, M. Ernzerhof, Generalized gradient approximation made simple. *Phys. Rev. Lett.* **77**, 3865–3868 (1996).
42. I. F. Momma Koichi, VESTA3 for three-dimensional visualization system for crystallographic studies and electronic state calculations. *J. Appl. Cryst.* **44**, 1272–1276 (2011).
43. K. Schwarz, P. Blaha, G. K. H. Madsen, Electronic structure calculations of solids using the WIEN2k package for material sciences. *Comput. Phys. Commun.* **147**, 71–76 (2002).
44. K. Schwarz, P. Blaha, Solid state calculations using WIEN2k. *Comput. Mater. Sci.* **28**, 259–273 (2003).
45. K. S. Peter Blaha, G. Madsen, D. Kvasnicka, J. Luitz, *WIEN2k User's Guide* (Vienna University of Technology, 2014).
46. C. Hébert, J. Luitz, P. Schattschneider, Improvement of energy loss near edge structure calculation using Wien2k. *Micron* **34**, 219–225 (2003).
47. C. Hébert, Practical aspects of running the WIEN2k code for electron spectroscopy. *Micron* **38**, 12–28 (2007).
48. M. O. Krause, Atomic radiative and radiationless yields for K and L shells. *J. Phys. Chem. Ref. Data Monogr.* **8**, 307–327 (1979).
49. H. Yun, M. Topsakal, A. Prakash, K. Ganguly, C. Leighton, B. Jalan, R. M. Wentzcovitch, K. A. Mkhoyan, J. S. Jeong, Electronic structure of BaSnO₃ investigated by high-energy-resolution electron energy-loss spectroscopy and ab initio calculations. *J. Vac. Sci. Technol. A* **36**, 031503 (2018).
50. J. M. Cowley, A. F. Moodie, The scattering of electrons by atoms and crystals. I. A new theoretical approach. *Acta Crystallogr.* **10**, 609–619 (1957).
51. E. J. Kirkland, *Advanced Computing in Electron Microscopy* (Springer, 2010).
52. R. F. Loane, E. J. Kirkland, J. Silcox, Visibility of single heavy atoms on thin crystalline silicon in simulated annular dark-field STEM images. *Acta Crystallogr. A* **44**, 912–927 (1988).
53. B. C. Chakoumakos, Systematics of atomic displacement parameters in perovskite oxides. *Phys. B Condens. Matter* **241**, 361–363 (1997).
54. J. S. Jeong, M. L. Odlyzko, P. Xu, B. Jalan, K. A. Mkhoyan, Probing core-electron orbitals by scanning transmission electron microscopy and measuring the delocalization of core-level excitations. *Phys. Rev. B* **93**, 165140 (2016).

Acknowledgments: We thank K. Ganguly and C. Leighton for providing high-pressure oxygen-sputtered samples. **Funding:** This work was supported in part by SMART, one of seven centers of nCORE, a Semiconductor Research Corporation program, sponsored by National Institute of Standards and Technology (NIST), and by National Science Foundation (NSF) through University of Minnesota (UMN) MRSEC under awards DMR-1420013 and DMR-2011401. This work used the UMN Characterization Facility, supported in part by the NSF through the UMN MRSEC program. The MBE growth work was supported partially by the NSF through DMR-1741801 and the Air Force Office of Scientific Research Program through grant no. FA9550-19-1-0245. **Author contributions:** H.Y. and K.A.M. conceived the project. H.Y. performed STEM experiments and Multislice simulations with inputs from J.S.J. and K.A.M. and ab initio calculations with inputs from M.T. and T.B. A.P. grew thin films by hybrid MBE with input from B.J. H.Y. and K.A.M. prepared the manuscript with contributions from all authors. K.A.M. directed all aspects of the project. **Competing interests:** The authors declare that they have no competing interests. **Data and materials availability:** All data needed to evaluate the conclusions in the paper are present in the paper and/or the Supplementary Materials. Additional data related to this paper may be requested from the authors.

Submitted 21 June 2020

Accepted 24 November 2020

Published 15 January 2021

10.1126/sciadv.abd4449

Citation: H. Yun, M. Topsakal, A. Prakash, B. Jalan, J. S. Jeong, T. Birol, K. A. Mkhoyan, Metallic line defect in wide-bandgap transparent perovskite BaSnO₃. *Sci. Adv.* **7**, eabd4449 (2021).